Physics – Uspekhi **67** (8) 814 – 827 (2024)

REVIEWS OF TOPICAL PROBLEMS

PACS numbers: 52.58.Lq, **52.59. – f**, 52.80.Qj

ON THE 90TH ANNIVERSARY OF THE P.N. LEBEDEV PHYSICAL INSTITUTE (LPI)

Coherent properties of high-current nanosecond discharge radiation

I N Tilikin, N V Pestovskii, S N Tskhai, T A Shelkovenko, S A Pikuz, S Yu Savinov

DOI: https://doi.org/10.3367/UFNe.2024.02.039642

Contents

Abstract. We consider the coherent properties of short-wavelength radiation generated by high-current nanosecond discharges. The first part of the paper is concerned with the feasibility of using a plasma soft X-ray radiation source, the X-pinch, proposed at the Lebedev Physical Institute in the late 1970s as part of the inertial thermonuclear fusion program based on high-current nanosecond discharges. Experimental studies of the X-pinch suggest that a high-temperature plasma with extreme parameters is produced in it, which emits a high-power electromagnetic pulse in a broad wavelength range, with the X-ray radiation source (1 keV < E < 10 keV) possessing unique parameters. Its dimensions are so small (< 1 μm) that the radiation it emits is spatially coherent. When it was used in projection radiography, phase contrast was observed in images of low-absorbing objects. The results of assessing the applicability of the wave approximation in image analysis and simulations of the intensity distribution in images using Fresnel integrals are presented. In the second part of the paper, we analyze a new physical phenomenon, also discovered at the Lebedev Physical Institute, related to the production of a short (< 2 ns), narrowly directed electromagnetic radiation pulse in the pre-breakdown stage of a high-current discharge on the surface of a ferrite, 50% of the energy spectrum of which lies in the X-ray region ($h\nu$ > 1 keV) with an energy of ∼ 0.6 mJ and average power of ∼ 0.3 MW. The pulse propagates parallel to the ferrite surface towards the anode with a low angular divergence of < 2°. The high radiation directivity in the absence of special optical devices and the quadratic dependence of the energy flux density transferred by a detected radiation pulse on the length of the working part of the ferrite prism indicate with a high probability its coherent nature. We discuss the possible mechanism for generating radiation, which involves the excitation of short-term magnetization of ferrite sections as a result of the passage of an exciting electromagnetic pulse over the surface of a ferrite prism during the formation of a longitudinal electric field in the interelectrode gap and subsequent coherent addition of elementary waves. The total radiation from the entire surface as a result of interference is concentrated in a small spatial region, which explains the high intensity and directionality of the radiation.

Keywords: X-pinch, high-current nanosecond discharges, soft X-rays, spatial and temporal coherence, phase contrast, low-divergence short electromagnetic pulses, short-term magnetization, ferrites

I N Tilikin [a], **N V Pestovskii** [b], **S N Tskhai** [c], **T A Shelkovenko, S A Pikuz** [d], **S Yu Savinov** [e]
Lebedev Physical Institute, Russian Academy of Sciences,
Leninskii prosp. 53, 119991 Moscow, Russian Federation
E-mail: [a] tilikin@sci.lebedev.ru, [b] pestovskii@sci.lebedev.ru,
[c] tskhai@sci.lebedev.ru, [d] pikuzsa@lebedev.ru,
[e] savinov@sci.lebedev.ru

Received 9 October 2023, revised 1 February 2024
Uspekhi Fizicheskikh Nauk **194** (8) 865 – 880 (2024)
Translated by E N Ragozin

1. X-pinch as a source of spatially coherent radiation

1.1 Introduction

At the end of the 1970s, at Lebedev Physical Institute (LPI), a start was made on investigations of high-current nanosecond Z-pinches as sources of high-temperature plasma for inertial controlled fusion. As part of this research, an original Z-pinch scheme was proposed in the Laboratory of Problems of New Accelerators of the LPI in 1982 which made it possible to effectively transfer the energy of an electric storage device into plasma at a given point in space and obtain matter with extreme parameters at a given point in time [1]. The original configuration consisted of two thin conductors crossed in a vacuum diode, to which a high-voltage pulse was supplied from a low-impedance high-current generator (Fig. 1).

In the first experiments, the current amplitude amounted to 120 kA with a rise rate of about 5 kA ns^{-1}. Subsequently, in the course of studies of the X-pinch, which turned out to be an extremely interesting physical subject, other modifications of

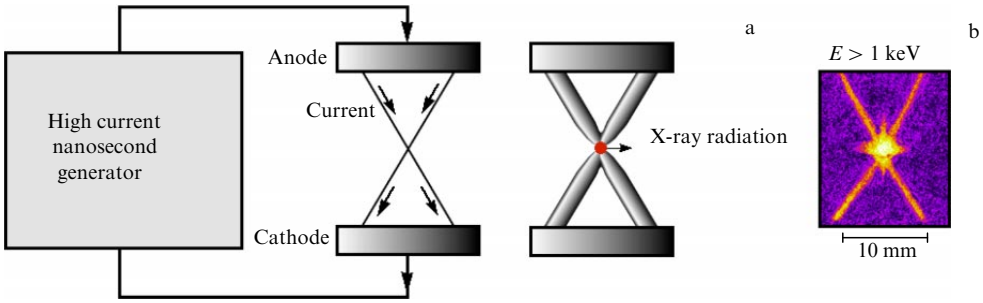

Figure 1. (a) Schematic representation of X-pinch, (b) time-integrated image of X-pinch in X-ray radiation with photon energies greater than 1 keV obtained using a pinhole camera.

the pinch appeared, whose configurations were often determined by the parameters of the generators powering the X-pinch as a load. To date, the X-pinch has been implemented in facilities with a loaded current of 40 kA to 5 MA and a current rise rate above 1 kA ns^{-1} with retention of its main properties: extreme plasma parameters and strict localization in space and time. A detailed review of X-pinch research, which is still ongoing in a number of laboratories around the world, is given in Refs [2, 3].

Even from the first results of experiments with the X-pinch, it became clear that the size of the plasma region emitting soft X-ray radiation with photon energies greater than 1 keV can be quite small in size. Obtaining real values of these dimensions required many years of research, since measurements repeatedly ran into the limits of the capabilities of the techniques used. This required not only improving standard techniques, but also inventing and using new ones, such a X-ray refractive optics and artificial three-dimensional diffraction-interference structures. Ultimately, it was shown that the so-called hot spot (HS) of the X-pinch can be micron-sized [4, 5]. In this case, the energy output of the radiation was at the level of fractions or even units of joules with a pulse duration $\sim$ 1 ns or even shorter [6, 7]. The resultant extreme parameters naturally attracted attention to the X-pinch as a radiation source for projection radiography of fast phenomena in matter with a high energy density [8]. In particular, unique studies of the nanosecond explosion of wires and wire assemblies were carried out, which made it possible to obtain reliable information about the processes during and after the explosion, which was previously unavailable. The short duration of the probing pulse makes it possible to study even such fast processes as the formation of a waist in the X-pinch itself, where an HS is formed in a time of less than 1 ns (Fig. 2).

The key parameter of the probing source in projection radiography is its size, which determines the spatial resolution of the object being imaged. The image contrast in the geometric (ray) optics approximation is determined by the difference in the absorption of X-ray radiation between neighboring areas of the imaged object. In many cases, the images of the objects under study were consistent with these assumptions. However, in a number of cases, the image contrast in the area of sharp changes in density was significantly higher than expected. This is an indication that factors related to the wave properties of the probing radiation come into play in image formation. In the proposed work, an analysis of image formation will be carried out in order to determine the feasibility of using the X-pinch as a source of spatially coherent radiation.

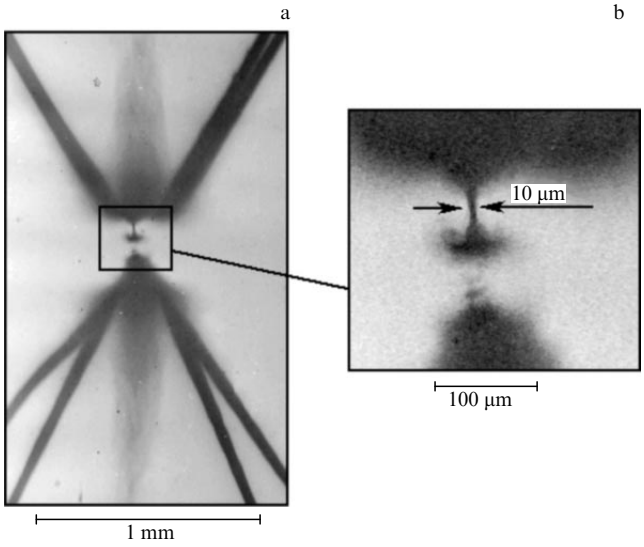

Figure 2. (a) X-ray image of waist of the X-pinch from four tungsten wires with a diameter of 19.8 μm at a time of about 300 ps before formation of HS. (b) Image detail in waist area. Exposure time is 20 ps, source of probing radiation is a similar X-pinch included in discharge circuit parallel to the one being studied.

1.2 Experimental results and their analysis

By way of example, Fig. 3 shows an image of an exploded tungsten wire 25 μm in diameter, which in the initial state was covered with a thin layer (5 μm) of polyimide insulation. In the case of an ideal point source, the line width in the image of the polymer shell at the indicated time would correspond to its thickness equal to $\Delta x = 5$ μm. In any case, the width of the recorded image definitely indicates that the size of the source does not exceed the specified value. The shell itself, taking into account the stretching during the expansion of the wire explosion products, can be much thinner. In this case, the calculation of radiation absorption in the shell substance yields a change in the blackening density of the photographic film that is significantly smaller than that observed in the experiment.

Consider a simple model (Fig. 4) of image formation. Let a source with a characteristic size D illuminate an object with some inhomogeneity of size h with radiation of wavelength λ. We also assume that the radiation incident on the detector produces an interference pattern on it. In this case, we do not consider the reason for the deflection of rays due to inhomogeneity, and we believe that there are no phase distortions.

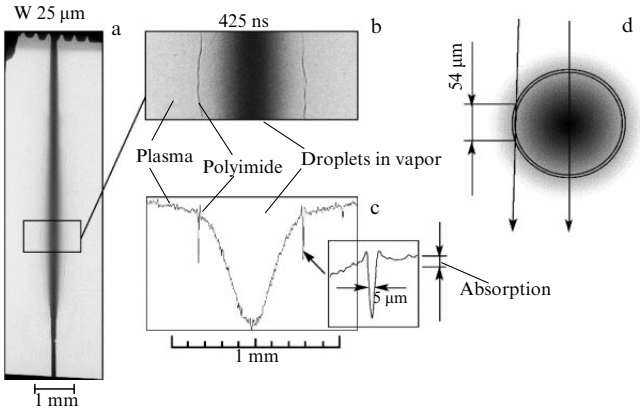

Figure 3. (a) X-ray image of an exploded 25-μm W-wire in polyimide insulation in radiation of 2×25-μm Nb X-pinch; (b) image detail; (c) densitogram of image in radial direction (indicated is the magnitude of blackening density jump of photographic film in the case of only radiation absorption in expanded shell); (d) schematic for calculating absorption.

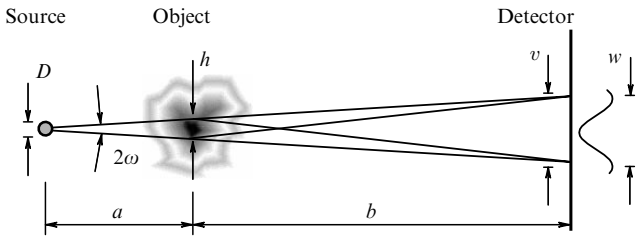

Figure 4. Schematic of interference and appearance of interference fringes during point projection.

According to Ref. [9], the criterion for the observability of interference fringes is given by the condition

$$D \tan \omega \leqslant \frac{\lambda}{4} . \tag{1.1}$$

For small angles $\omega = h/2a$, and the condition will be of the form

$$D \leqslant \frac{a\lambda}{2h} . \tag{1.2}$$

The width of the interference fringes is

$$w = \frac{b\lambda}{h} . \tag{1.3}$$

The size of the image on the detector in the point projection scheme in the ray approximation is

$$v = h\left(1 + \frac{b}{a}\right) = \frac{hb}{a} , \quad \text{if} \quad b \gg a . \tag{1.4}$$

It is reasonable to put $v = w$. Then, by combining expressions (1.3) and (1.4), we obtain

$$a\lambda = h^2 . \tag{1.5}$$

This relationship exactly corresponds to the diffraction resolution criterion $\Delta x_{\text{diff}} = h \sim \sqrt{a\lambda}$ [2]. We compare expressions (1.1) and (1.5) to obtain the following criterion:

$$D \leqslant \frac{h}{2} . \tag{1.6}$$

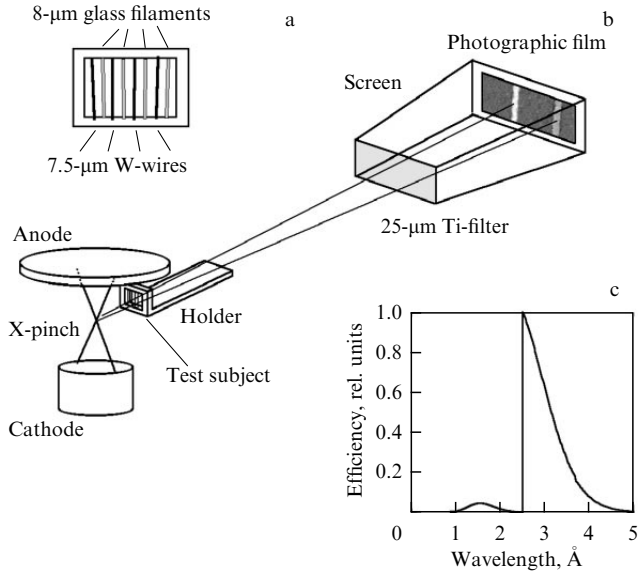

Figure 5. High-magnification X-ray imaging experiment; (a) design of test subject, (6) experiment layout, (c) radiation wavelength range involved in image formation.

The fact that, in the approximation used, the criterion for the visibility of interference fringes in this case does not depend on the wavelength suggests that the most important parameter is the size of the source, while the monochromaticity of the radiation does not play a significant role. If criterion (1.6) is met, at least one fringe should be visible even with a very broad spectrum. However, we should not forget that the fringe width must be experimentally recordable, i.e., the characteristic size of the inhomogeneity of the object on which the interfering rays are deflected must be quite small.

A complete analysis of images with the inclusion of the wave properties of the probing radiation required the use of calculations of Fresnel–Kirchhoff integrals taking into account the functions of object transmission and wave propagation in space, as well as staging special experiments [2, 5]. In particular, images of opaque and semi-transparent wires and fibers were studied with a very high magnification (> 50), which made it possible to eliminate the factor of spatial resolution of the radiation detector (photographic film). The experimental setup and an example of the resulting image are shown in Figs 5 and 6.

Figures 7 and 8 display the results of our analysis of experimental images of glass fibers and tungsten wires. Figure 7 shows the radiation intensity distributions of a point source in the plane of the screen for two wavelengths. In the case of a tungsten wire, almost only the period of oscillations near the edge of the image changes, while, in the image of a glass fiber, their amplitudes and positions of the maxima also change. Averaging the two images leads to a rapid attenuation of the oscillations; however, the first period is visible quite clearly. To compare theory and experiment, calculations were made of the distribution of radiation intensities from a source with different sizes for three wavelengths (2.5, 3, and 3.5 Å), which were averaged with weighting factors corresponding to the detection efficiency curve shown in Fig. 5c.

We assume that the spatial distribution of the source radiation intensity is Gaussian:

$$B(x_s) = \left(\frac{1}{s\sqrt{\pi}}\right) \exp\left(-\frac{x_s^2}{2s^2}\right) . \tag{1.7}$$

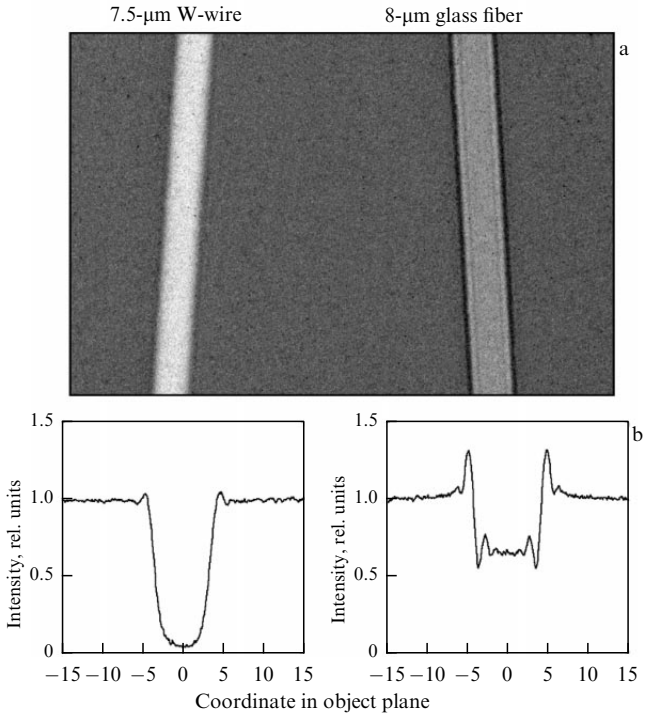

Figure 6. Negative images of a glass fiber and a W-wire with an 82× magnification in the radiation of 2 × 25-μm Nb X-pinch.

The calculation results are plotted in Fig. 8. The specified values of the s parameter are related to the size of the source as follows:

$$D_{\mathrm{FWHM}} = 2\sqrt{2}\,\ln 2s = 2.35s\,. \tag{1.8}$$

The bold lines show the distributions that most closely match the experiment.

In this approximation, it was not possible to achieve complete compliance, especially for glass fibers, so the choice of the compliance criterion was important. This criterion was chosen to be the number of oscillations visible in the image, which seems more reliable than, for example, the ratio of amplitudes, whose measurement calls for careful calibration of the entire imaging system. In addition, we did not know the exact chemical composition of the glass fibers. The function of brightness distribution over the cross section of the source was also unknown. However, we can state with confidence that the size of the radiating region of the Nb X-pinch, which was used in the described experiment, did not exceed 0.9–1 μm.

The size of the smallest resolvable element of the imaged object can also be estimated from the radius of the first Fresnel zone for a given experimental geometry. The radius of the first Fresnel zone is determined by the formula [9]

$$r_1 = \left(\frac{ab}{a+b}\right)^{1/2} \lambda^{1/2}\,. \tag{1.9}$$

For $b \gg a$, the formula gives the same well-known estimate $\Delta x = (a\lambda)^{1/2}$ of the diffraction resolution limit. A

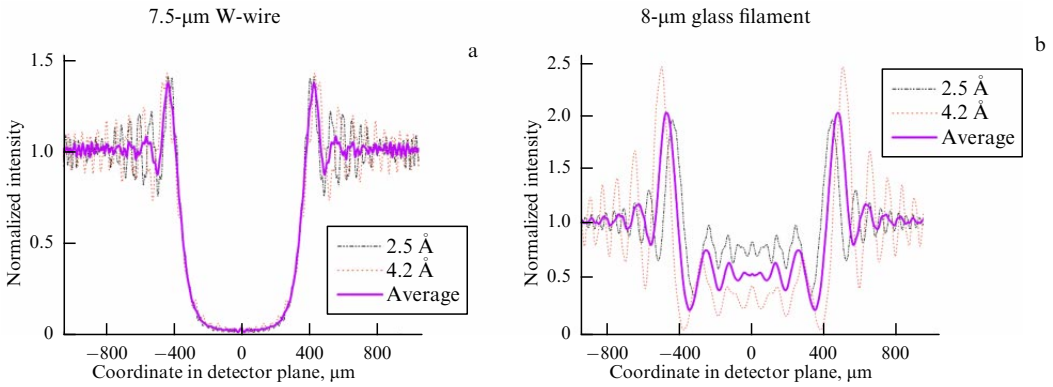

Figure 7. Calculated radiation intensity distribution in detector plane depending on spectrum of probing radiation.

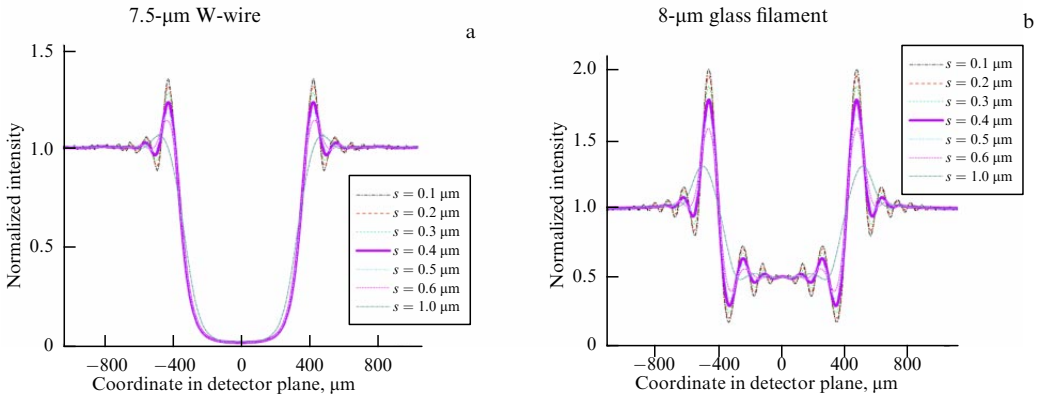

Figure 8. Calculated radiation intensity distribution in detector plane depending on size of radiation source. Parameter s is related to source half-width as $D_{\mathrm{FWHM}} = 2\sqrt{2}\ln 2s = 2.35s$.

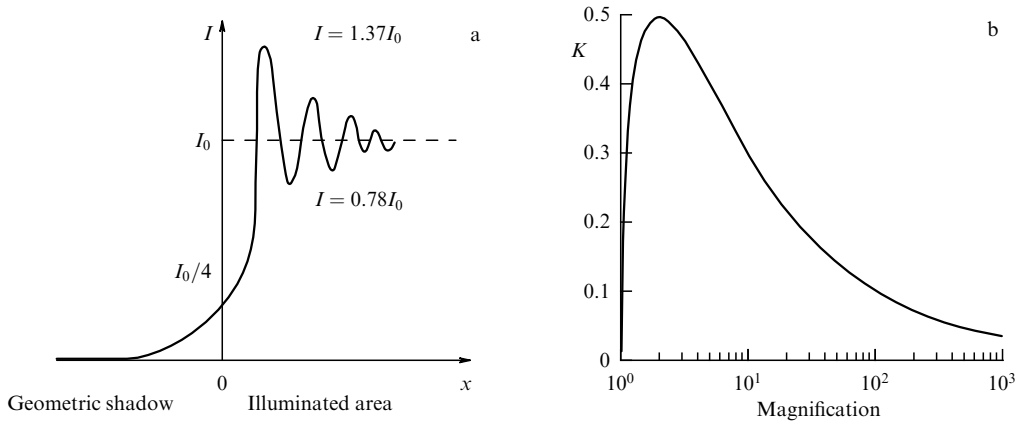

Figure 9. (a) Radiation intensity in diffraction at edge of slit; (b) dependence of coefficient K on magnification.

rigorous calculation of the radiation intensity in the diffraction at the straight edge of a screen gives the dependence shown in Fig. 9. In this case, the distance from the geometric position of the screen edge (0 along the abscissa axis) to the first maximum $\Delta x = 0.85\lambda^{1/2}W$, where $W = (ab/(a+b))^{1/2}$.

To summarize, we note that the important parameters of the experiment in practice are the magnification $M = (a+b)/a$ and the distance from the radiation source to the detector $l = a + b$, which largely determines the sensitivity of the system. Formula (1.9) can be rewritten as follows:

$$r_1 = \Delta x = (\lambda l)^{1/2} K, \tag{1.10}$$

where

$$K = \frac{(M-1)^{1/2}}{M}\,.$$

The dependence of the K coefficient on magnification is plotted in Fig. 9b. This dependence is useful for the practical use of the X-pinch as a source of spatially coherent X-ray radiation. It shows that the wave properties of radiation manifest themselves most strongly (all other things being equal) when the object under study is located in the middle between the source and the detector. In projection radiography, this arrangement corresponds to a twofold magnification. In this case, the phase contrast of the images is most pronounced, and the density gradients of the objects under study are well determined in them, even when the differences themselves are small. In cases where the wave properties of radiation are an interfering factor and it is necessary to obtain the best spatial resolution, either high magnification factors or the contact technique, when the object 'lies' on the detector and the magnification is equal to unity, must be used. In the former case, the spatial resolution of the detector does not matter much, since the image element can always be made larger than the detector element. In addition, the object has no physical contact with either the source or the detector and therefore can be of a dynamic explosive nature, which is characteristic of matter with a high energy density. In the case of contact radiography, spatial resolution is determined only by the parameters of the detector, so that obtaining high-resolution images is a special task, and recording fast processes is completely out of the question.

2. Generation of coherent X-ray radiation at initial stage of high-current surface breakdown of ferrite

2.1 Introduction

In the course of studies of VUV radiation from the plasma of a high-current discharge on the surface of a ferrite [10, 11], at its initial stage, we discovered the generation of a short, narrowly directed pulse of fairly hard radiation ($h\nu > 500$ eV) [12]. The brightness of this radiation significantly (by more than an order of magnitude) exceeded the brightness of the ferrite surface radiation measured in Refs [10, 11].

The production of X-rays from electrical discharges is now well known. For instance, in Ref. [13], an X-ray pulse was recorded in the study of Formed-Ferrite-Flash Plasma (FFFP) (initial voltage of ~ 30 kV, discharge gap length of 14.5 cm). Its production began ~ 2 μs before the start of the high-current phase of the discharge, i.e., in the mode of heating the amorphous channel on ferrite, and abruptly ended with the beginning of the high-current phase. In this mode, intense electron-ion emission occurred; electrons, when entering a strong electric field, formed fast electron beams, which excited high-energy states of atoms and ions with the subsequent emission of X-rays. This radiation was observed in Ref. [13] perpendicular to the ferrite surface and did not have a clearly defined directionality.

X-ray production occurs not only during surface breakdowns. Specifically, in Refs [14, 15], X-ray emission was observed in the pre-breakdown stage of pulsed atmospheric discharges caused by runaway electrons. In Ref. [16], intense X-ray radiation was detected in a meter-long megavolt atmospheric discharge, and a model of electron acceleration with subsequent generation of X-ray photons due to bremsstrahlung was proposed. In Ref. [17], it was first discovered that X-ray bremsstrahlung during a megavolt nanosecond breakdown of atmospheric air is characterized by a fairly high directivity (angular divergence of $\sim 10^\circ$).

Note that the production of X-ray radiation, which was previously observed in discharges of various types, was associated with the formation of fast electron beams. In the case described in Ref. [12], we discovered a physical phenomenon of a different nature, when the observed X-ray radiation was not caused by the passage of high-energy electrons through the discharge gap. This paper presents the first

results of a study of this phenomenon and their possible interpretation.

2.2 Experimental and diagnostic techniques

The experiments were performed on a BIN generator with an output current amplitude of up to 270 kA and a rise time of 100 ns [2]. The impedance of the generator's forming line was $\sim 1\ \Omega$, and the voltage at the generator output in the experiments amounted to 240 kV, with the charging voltage of the forming line being about 350 kV. The generator load was a rectangular prism made of ferrite (Ni–Zn)Fe_2O_4 grade M1000NN with transverse dimensions of 10×20 mm. The prism was mounted orthogonal to the diode axis, as shown in Fig. 10a. By changing the length of the electrode on the cathode side, it was possible to vary the length of the working part of the ferrite prism from 1.5 cm to 7 cm. The path of current flow along the surface of the ferrite was defined by a line drawn with a graphite pencil. This path is generally preserved during a series of sequential discharges [10, 11]. The generator load was not matched and its impedance varied greatly during the pulse. The pressure in the discharge chamber did not exceed 10^{-4} Torr.

The discharge radiation intensity was measured by calibrated diamond detectors with photoconductivity (Photo-Conductive Detectors, PCDs), which have a flat dependence of the spectral responsivity on the photon energy in the range from 10 eV to 10 keV, equal to $C = 5 \times 10^{-4}$ A W^{-1}. In the high-energy region, the sensitivity smoothly decreases in accordance with the carbon absorption curve [18]. The dimensions of the detector crystals were $\sim 3 \times 1$ mm in the transverse direction and 0.5 mm in the detection direction, which ensured sufficient responsivity of the detectors up to 10 keV with a constant spectral responsivity in the range of 10 eV–5 keV. The response time of the detectors was less than 0.3 ns. The total time resolution of the recording path, taking into account the bandwidth of the Tektronix TDS 3104B oscilloscope and cable lines, was ~ 2 ns. The detectors, as a rule, were located at a distance of 26 cm from the ferrite end at different angles relative to the discharge direction (x-axis in Fig. 10a).

The layout of the detectors is shown in Fig. 10a. The radiation detection angles varied in the xy plane of the ferrite surface (azimuthal angle $-8° < \theta < +22°$) and in the xz plane orthogonal to the ferrite surface (polar angle $-1° < \alpha < +5°$). To record cross sectional images of the generated radiation, use was made of Fuji BAS TR memory plates, sensitive to both X-ray and UV radiation, located at a distance of 26 cm from the end of the ferrite. To eliminate the influence of UV radiation from a high-current discharge plasma on the ferrite surface [11], aluminum foil filters were used. The time dependence of the load current was determined by numerical integration of the signal from a Rogowski coil (bandwidth > 500 MHz), and the output voltage on the diode was measured by a resistive-capacitive divider.

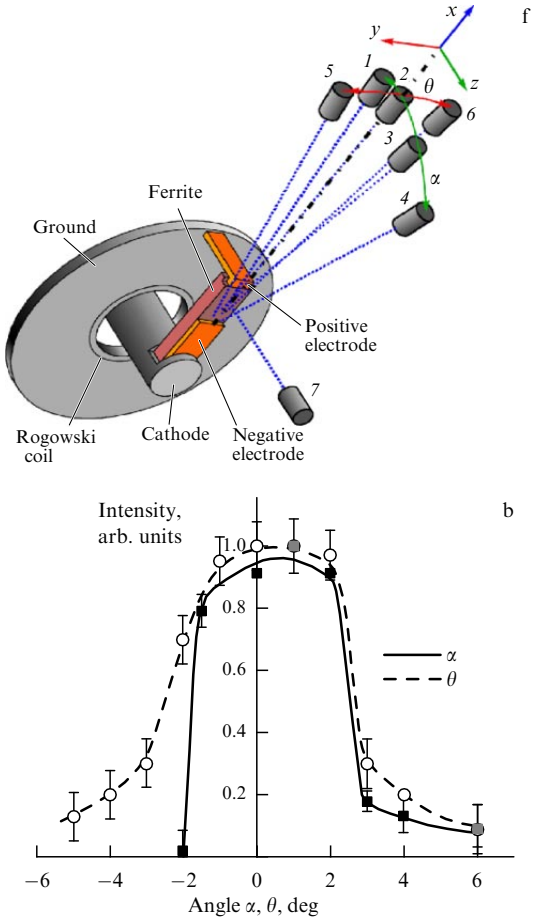

Figure 10. (a) Layout of experiment for studying radiation of ferrite. *1*–*7* — orientation of detectors. (b) Angular dependences of intensity of ferrite radiation under study.

2.3 Experimental results

The time dependences of voltage, discharge current, and radiation intensities recorded along and perpendicular to the direction of the ferrite surface (PCD in positions 2 and 7) are shown in Fig. 11. The dependence of the first time derivative of voltage, which characterizes the rate of voltage increase, is also presented here. Experimental conditions: length of the working part of the ferrite prism $l = 6.5$ cm, one detector was located parallel to the working surface of the prism at distance $L = 26$ cm from its end, the other was perpendicular to the working surface at distance $L_\perp = 26$ cm from it.

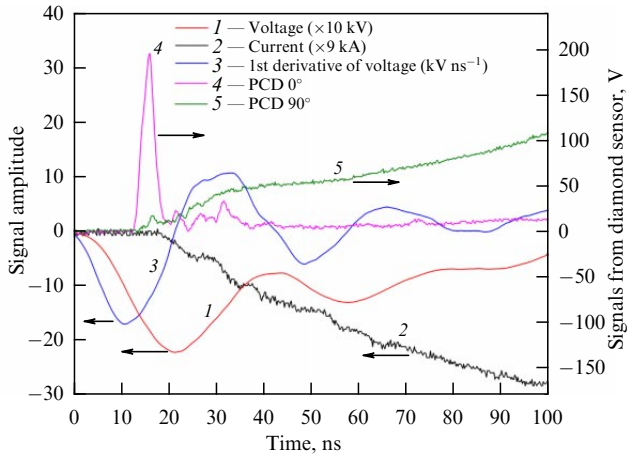

Figure 11. Time dependences of voltage (*1*), discharge current (*2*), first time derivative of voltage (*3*), and radiation intensities recorded along (*4*) and perpendicular (*5*) to direction of ferrite surface (positions of detectors *2* and *7* in Fig. 10a). One detector was located parallel to working surface of the prism at distance $L = 26$ cm from its end, the other was perpendicular to working surface at distance $L_\perp = 26$ cm from it.

One can see from Fig. 11 that, in the initial (pre-breakdown) stage of the discharge, when there is no discharge current yet, a short ($\tau < 2$ ns) pulse of ionizing radiation is observed in the direction of the discharge axis, the intensity of which is more than an order of magnitude higher than the intensity of the radiation recorded at the same points in time in the perpendicular direction. Note that the actual duration of the signal may be shorter, since the measured duration coincides with the temporal resolution of the recording path. We also note that the onset of the indicated radiation pulse coincides in time with the maximum of the first derivative of the voltage with respect to time, i.e., at the point where the rate of voltage rise is highest (the inflection point on the voltage versus time curve). The discharge current at this moment is zero, the voltage continues to increase, and finally, in the vicinity of the applied voltage peak, a discharge current appears and a breakdown of the discharge gap develops.

Also studied were the angular dependences of the radiation intensities. The radiation detectors were located at a distance $L = 15$ cm from the end of the prism of length $l = 2$ cm. The measurement results are presented in Fig. 10b. It can be seen that the radiation under study is concentrated in an area with angular dimensions of $\sim 4^\circ$ in a plane perpendicular and $\sim 5^\circ (\pm 2.5^\circ)$ in a plane parallel to the working surface of the ferrite prism. Considering that the angular resolution is $\sim 2^\circ$ in the measurement geometry involved, the presented results should be considered to be estimates.

Possible, in principle, in discharge experiments carried out at such high voltages (100–300 kV) is the production of high-energy electron beams [19, 20], which, when interacting with recording devices, produce an effect similar to that of high-energy photons. Therefore, experiments were carried out to prove that the observed phenomena are caused precisely by hard electromagnetic radiation. First of all, the transmittance of a 50-μm Al filter and a 10-μm Be filter was measured (see below for details). Such measurements in the case of an electron beam make it possible to estimate its average energy [21]. In the case under study, for Al ($I_{Al} = 0.09 \times I_0$, where I_0 is the intensity in the absence of filters), the electron energy should be at the level $E_e = 95$ keV, and for Be ($I_{Be} = 0.56 \times I_0$), $E_e = 55$ keV, i.e., there is a noticeable discrepancy.

The next series of experiments was carried out under conditions where a permanent magnet with transverse dimensions of 10×25 mm was located at the end of the ferrite prism to produce a constant magnetic field of intensity $H = 700$ G. Estimates show that, with electron beam energy $E_e = 100$ keV, the beam displacement should be $\Delta y \approx 20$ cm, and with electron beam energy $E_e = 50$ keV, $\Delta y \approx 32$ cm. Our measurements (see Fig. 10) using diamond detectors showed that pulse-to-pulse fluctuations in the amplitude of the emission peak ranged up to 20% in a series of consecutive experiments. When a magnetic field $H = 700$ G appears, no effect greater than these random intensity fluctuations is observed. The existence of narrowly directed electromagnetic radiation during breakdown above the ferrite surface was also confirmed by us with other parameters of the applied voltage: an amplitude of ~ 300 kV and rise front of ~ 1 ns [22]. It can therefore be considered proven that we are indeed dealing with fairly hard electromagnetic radiation.

The spectral composition of the radiation pulse was estimated. For this purpose, the integral intensities I_{Al}, I_{Be}, and I_{PP} behind aluminum, beryllium, and polypropylene filters were measured: Al: $d = 50$ μm, $h\nu > 4$ keV, ($\lambda \leqslant 2.5$ Å), $I_{Al} = 0.09 \times I_0$; Be: $d = 10$ μm, $h\nu > 0.5$ keV, $I_{Be} = 0.56 \times I_0$; PP (C_3H_6-polypropylene) $d = 4$ μm, $0.1 \leqslant h\nu \leqslant 0.293$ keV ($124 \leqslant \lambda \leqslant 42.4$ Å), $I_{PP} = 0.66 \times I_0$. Here, I_0 is the integral intensity recorded by the detector in the absence of filters, i.e., integral intensity in the photon energy range $10^{-2} \leqslant h\nu \leqslant 10$ keV ($1.24 \leqslant \lambda \leqslant 1241$ Å). The measurement results make it possible, using a database on the transmission of various materials [23], to estimate the spectral composition of the radiation under study. The table presents the results of such an estimate, and Fig. 12 shows the dependences of the spectral densities of the intensity of the radiation under study on the photon energy in the range $10^{-2} \leqslant h\nu \leqslant 10$ keV.

Table 1. Fraction of radiation intensity in different energy ranges. Measurement error (electrical noise and possible background radiation) did not exceed 10%.

Quantum energy $h\nu$	Radiation intensity
$h\nu > 10^{-2}$ keV ($\lambda \leqslant 1240$ Å)	100%
$10^{-2} \leqslant h\nu \leqslant 0.1$ keV ($124 \leqslant \lambda \leqslant 1241$ Å)	10%
$0.1 \leqslant h\nu \leqslant 0.293$ keV ($42 \leqslant \lambda \leqslant 124$ Å)	22%
$0.293 \leqslant h\nu \leqslant 0.5$ keV ($25 \leqslant \lambda \leqslant 42$ Å)	7%
$0.5 \leqslant h\nu \leqslant 1$ keV ($12.4 \leqslant \lambda \leqslant 25$ Å)	10%
$1 \leqslant h\nu \leqslant 4$ keV ($3.1 \leqslant \lambda \leqslant 12.4$ Å)	26%
$4 \leqslant h\nu \leqslant 10$ keV ($1.2 \leqslant \lambda \leqslant 3.1$ Å)	2%

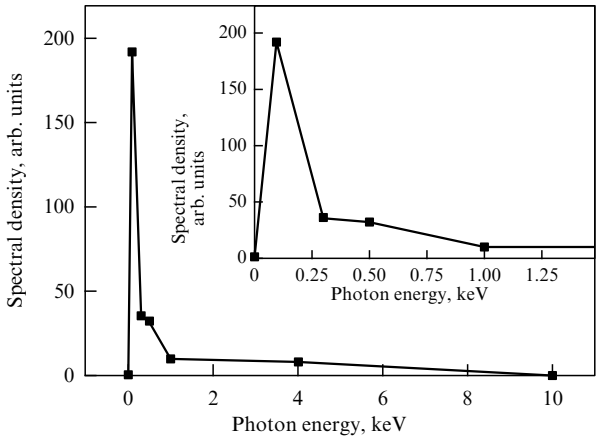

Figure 12. Spectral density of radiation intensity versus photon energy.

It follows from Table 1 that the X-ray range $E > 1$ keV ($\lambda < 12.4$ Å) accounts for 50% of the radiation energy spectrum and most of the UV radiation has an energy above 100 eV. Note that the radiation from the discharge, measured in the perpendicular direction from the ferrite surface, lies in the range of 10–800 eV [10, 11].

An independent estimate of the angular distribution of the radiation under study was carried out using the cross-sectional image of the generated beam. Images in the photon energy ranges determined by aluminum filters with thicknesses of 4 μm and 15 μm were recorded on Fuji BAS TR storage plates placed at a distance of $L = 26$ cm from the end of the ferrite prism with the length of the working part $l = 4.5$ cm.

The results are presented in Fig. 13. The image densitograms (Figs 13b–d) correspond to the time-integrated

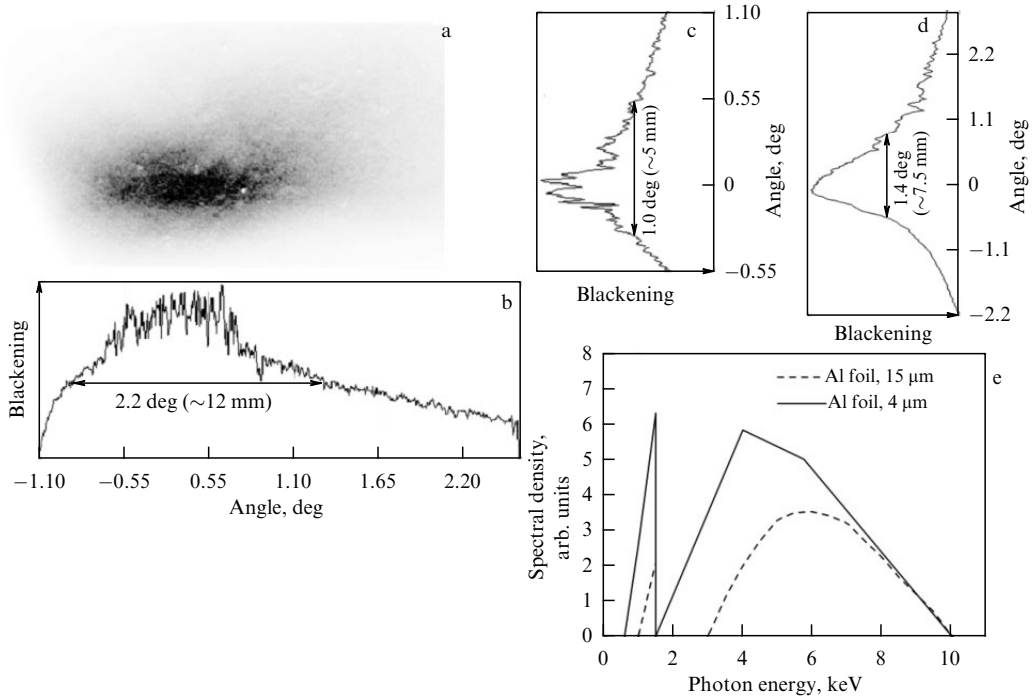

Figure 13. (a) Image of cross section of radiation beam on a Fuji BAS TR storage plate placed at distance $L = 26$ cm from end of ferrite prism behind an Al filter ($d = 15$ μm) with working area length $l = 4.5$ cm. (b) Angular dependence of plate blackening along image behind an Al filter ($d = 15$ μm). (c) Angular dependence of plate blackening across image behind an Al filter ($d = 15$ μm). (d) Angular dependence of plate blackening across image behind an Al filter ($d = 4$ μm). (e) Spectral radiation densities behind Al filters with $d = 4$ μm (solid curve) and 15 μm (dashed curve).

radiation energy absorbed by the plate emitted in this direction. One can see from the figure that the longitudinal section of the radiation beam behind an Al filter ($d = 15$ μm) is characterized by an angular size $\Delta\theta \sim 2.2°$ (linear size $a \sim 1.2$ cm), comparable to the transverse size of the ferrite (2 cm). The transverse angular size of the beam behind the Al filter ($d = 15$ μm) is $\Delta\alpha \sim 1.0°$ (linear size $b \sim 0.5$ cm). When using an Al filter ($d = 4$ μm), the dimensions of the longitudinal section of the beam remained virtually unchanged, but the cross section increased (Fig. 13d) and amounted to $\Delta\alpha \sim 1.4°$ (linear size $b \sim 0.75$ cm). A comparison of the spectral densities of radiation behind Al filters with $d = 4$ μm and 15 μm (Fig. 4e) shows that, in the transmitted radiation for $d = 4$ μm, the proportion of low-energy quanta is noticeably greater than for $d = 15$ μm.

The energy characteristics of the radiation under study were investigated. The total energy ε recorded by the detector is determined as follows:

$$\varepsilon = \frac{1}{CR}\int_{-\infty}^{\infty} V(t)\,\mathrm{d}t\,. \tag{2.1}$$

Here, R is the load resistance of the detector (in our case $R = 75\ \Omega$), $V(t)$ is the instantaneous signal magnitude measured in volts at the point in time t, and C is the detector responsivity (in our case $C = 5 \times 10^{-4}$ A W^{-1}). The duration of the radiation under study may turn out to be significantly shorter than the time resolution of the recording path $\tau_r \sim 2$ ns, and it is impossible to determine the pulse duration and its shape only from electrical measurements. Nevertheless, since the spectral width of the signal (see Table 1) barely exceeds the spectral sensitivity domain of the detector (quantum energy range from 10 eV to 10 keV), relation (2.1) can be used to estimate the total energy incident on the detector. The value $\int_{-\infty}^{\infty} V(t)\,\mathrm{d}t$ was determined as the area under the $V(t)$ curve (see Fig. 11). During the measurements, the length of the working area of ferrite l varied from 1.5 cm to 7 cm by changing the size of the negative electrode. In several series of experiments, the length of the working area first increased (2; 3; 5; 6; 7 cm) and then decreased (6.5; 5.5; 4.5; 3.5; 2.5; 1 cm). For each length, 2 to 3 consecutive shots were fired in each series. In this case, the total length of the ferrite sample did not change.

In the cases under study, the size of the detector crystals in the transverse direction ($r_D \sim 0.3$ cm, area: $S_D = 3 \times 10^{-2}$ cm^2) is just over half the smallest transverse size of the beam cross section recorded behind an Al filter ($d = 15$ μm); accordingly, the signal recorded by the detector is proportional to the energy flux density P transferred by the radiation pulse under study:

$$P = \frac{\varepsilon}{S_D}\,. \tag{2.2}$$

In Figure 14, the squares represent the measured dependence of the radiation energy flux density P on the length of the ferrite working area.

It follows from Fig. 14 that the radiation energy flux density P increases nonlinearly with ferrite length; the growth rate increases with increasing ferrite length. The line in the figure corresponds to the approximation of experimental data by the quadratic dependence of the energy flux density on the length of the ferrite working area. For the case under consideration, the proposed model (quadratic dependence) is reliable with probability $W > 0.87$. The maximum value of the flux density P with a discharge gap length of 7 cm was ~ 1 mJ cm^{-2}. To estimate the total energy ε transferred by a pulse of the radiation under study, we use the relation

$$\varepsilon = PS\,, \tag{2.3}$$

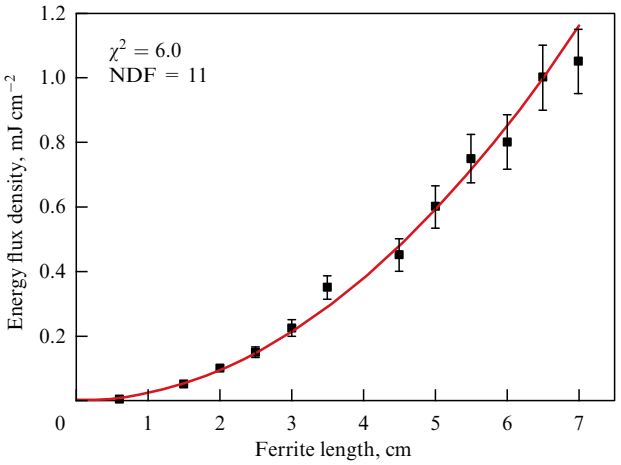

Figure 14. Dependence of radiation energy flux density P on length of discharge gap. Recording along ferrite surface (radiation detector in position *2* in Fig. 10a).

where S is the cross-sectional area of the beam. The cross section was considered to be a rectangle with dimensions $a = 1.2$ cm (width) and $b = 0.5$ cm (height) (the smallest size recorded behind the Al filter ($d = 15$ μm)). The maximum radiation energy for a discharge gap length of 7 cm was ~ 0.6 mJ, and the average power was 0.3 MW.

2.4 Discussion of experimental results

What is the physical cause of the observed radiation? In view of the sharp asymmetry in the angular distribution of radiation intensity in the absence of focusing and limiting devices, it can be assumed that the radiation is coherent and the asymmetry in the spatial distribution is due to interference phenomena. Only in the case of coherence of electromagnetic radiation can a narrowly directed beam be obtained in the absence of special optical elements.

Interference phenomena lead to the formation of a preferential direction of radiation propagation, and interference phenomena are impossible for incoherent radiation. By way of example, we can demonstrate a simple reasoning based on the theory of partial coherence [24].

Consider some surface σ, which consists of identical emitters emanating electromagnetic waves of the same amplitude, and some observation point P (Fig. 15). Let us assume that the radiation source is stationary and emits radiation of constant intensity over time. Let $V(t)$ be the complex amplitude of the intensity of the electromagnetic wave $E(t)$, i.e., $E(t) = 1/2(V(t) + V^*(t))$, where $V^*(t)$ is the complex conjugate of $V(t)$. For simplicity, let us abstract, as was done in a number of cases in Ref. [24], from the polarization properties of the radiation.

Let's divide the surface σ into N small areas. Let $s_1, s_2, \ldots, s_k, \ldots, s_N$ be the distances from these areas to point P. Let $V_1(t), V_2(t), \ldots, V_k(t), \ldots, V_N(t)$ be the values of the electric field amplitudes at P. Then, the electric field at this point can be calculated using the superposition principle as

$$V(t) = \sum_{k=1}^{k=N} \frac{V_k\bigl(t - (s_k/c)\bigr)}{s_k} \,. \tag{2.4}$$

The intensity I at point P can be calculated as

$$I = \bigl\langle V(t)V^*(t)\bigr\rangle \,, \tag{2.5}$$

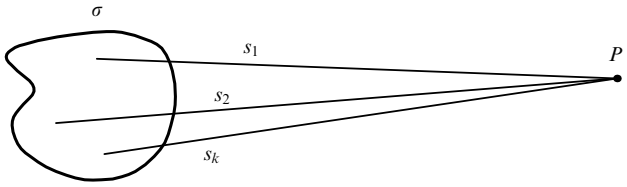

Figure 15. Radiating surface and observation point P.

where $\langle \ldots \rangle$ means time averaging, and from expression (2.5) it follows that

$$I = \left\langle \sum_{k=1}^{k=N} \frac{V_k\bigl(t - (s_k/c)\bigr)}{s_k} \sum_{m=1}^{m=N} \frac{V_m^*\bigl(t - (s_m/c)\bigr)}{s_m} \right\rangle . \tag{2.6}$$

Expression (2.6) has two components:

$$I = \sum_{k=1}^{k=N} \frac{\bigl\langle \bigl|V_k\bigl(t - (s_k/c)\bigr)\bigr|^2 \bigr\rangle}{s_k^2} + \sum_{k=1}^{k=N} \sum_{m=1}^{m=N} \frac{\bigl\langle V_k\bigl(t - (s_k/c)\bigr) V_m^*\bigl(t - (s_m/c)\bigr)\bigr\rangle}{s_k s_m} \,. \tag{2.7}$$

Here and further, $k \neq m$.

The terms in expression (2.7) of the form $\langle |V_k(t - (s_k/c))|^2\rangle/s_k^2$ are the radiation intensities of different areas of the surface at point P: $I_k = \langle |V_k(t - (s_k/c))|^2\rangle/s_k^2$. The terms of the form $\langle V_k(t - (s_k/c))V_m^*(t - (s_m/c))\rangle/s_k s_m$ are those that describe the interference between the waves emitted by different parts of the surface. If the waves from these areas are not coherent, time averaging gives $\langle V_k(t - (s_k/c))V_m^*(t - (s_m/c))\rangle/(s_k s_m) = 0$, and their contribution to expression (2.7) vanishes. Then,

$$I = \sum_{k=1}^{k=N} I_k \,. \tag{2.8}$$

Could a sharp angular anisotropy occur in this case? No, since, according to the condition, the radiation amplitude of each surface area is the same and does not change with time, the time shift $t - s_k/c$ does not change the value of I_k. The difference may be introduced by the $1/s_k^2$ factor, but if we consider the geometry of our experiment, the distances differ only slightly from each other. Consequently, with a incoherent addition of waves, a generally uniform illumination should be observed in a sufficiently large vicinity of point P.

A completely different situation occurs if the contribution

$$\sum_{k=1}^{k=N} \sum_{m=1}^{m=N} \frac{\bigl\langle V_k\bigl(t - (s_k/c)\bigr) V_m^*\bigl(t - (s_m/c)\bigr)\bigr\rangle}{s_k s_m}$$

is significant.

It is responsible for interference processes [24], since each term of this sum depends on the difference among the paths of rays from different areas of the surface. If the phases of electromagnetic oscillations emitted by different parts of this surface are correlated, i.e., if the waves are coherent, this contribution (interference term) causes a significant restructuring of the picture in the screen area. It can be shown that, due to the difference among the paths of coherent rays emitted by different parts of the ferrite, a pattern of spatial radiation intensity distribution close to the experimental one is observed. It is clear that it cannot arise in any other case.

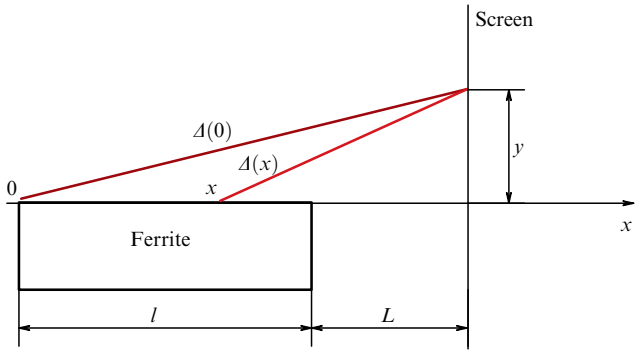

Figure 16. Observation scheme.

Consider, as an example, a situation in which the ferrite surface in our experimental configuration emits incoherent radiation. The geometry of the experiment is shown in Fig. 16.

According to expressions (2.7) and (2.8), in this case,

$$I = \sum_{k=1}^{k=N} \frac{\left\langle \left| V_k\left(t - (s_k/c)\right)\right|^2 \right\rangle}{s_k^2} ,$$

where

$$s_k = \Delta(x) = \left[(L + l - x)^2 + y^2\right]^{1/2} \approx L + l - x + \frac{1}{2L}\, y^2 ,$$

subject to $l, x, y \ll L$. Since we are considering a source stationary in time, the time dependence can be omitted, i.e.,

$$\left\langle \left| V_k\left(t - \frac{s_k}{c}\right)\right|^2 \right\rangle = I_0 = \text{const} .$$

Therefore,

$$I = I_0 \int_0^l \left(L + l - x + \frac{1}{2L} y^2\right)^{-2} \mathrm{d}x = \frac{I_0 l}{\left(L + l + (1/2L) y^2\right)\left(L + (1/2L) y^2\right)} . \qquad (2.9)$$

The result of the calculation using formula (2.9) for $l = 45$ mm and $L = 260$ mm is shown in Fig. 17. One can see from the figure that, even at a distance of ~ 100 mm from the axis along which the ferrite surface runs, the intensity changes by no more than 30%. Therefore, if the radiation from the ferrite surface were incoherent, no narrow directionality would be obtained.

We encounter a sharp asymmetry in the angular distribution of radiation intensity in the absence of focusing and limiting devices, for example, when Cherenkov radiation occurs: coherent radiation of optically transparent media caused by a charged particle moving in a medium at a speed exceeding the speed of light propagation in this medium [25–27].

What takes place in our case? Let us make the following assumption. In the pre-breakdown stage of the discharge, when a high voltage is applied to the cathode, a longitudinal electric field **E** is formed in the interelectrode gap, and a displacement current with density $\mathbf{J}_{\text{off}} = (1/4\pi)(\partial\mathbf{E}/\partial t)$ arises, which causes the formation of a magnetic field in the direction perpendicular to $\mathbf{J}_{\text{off}}$ and normal to the ferrite surface **n**. A powerful magnetic field pulse thereby passes through the discharge gap. This pulse, when passing through the discharge gap, causes short-term

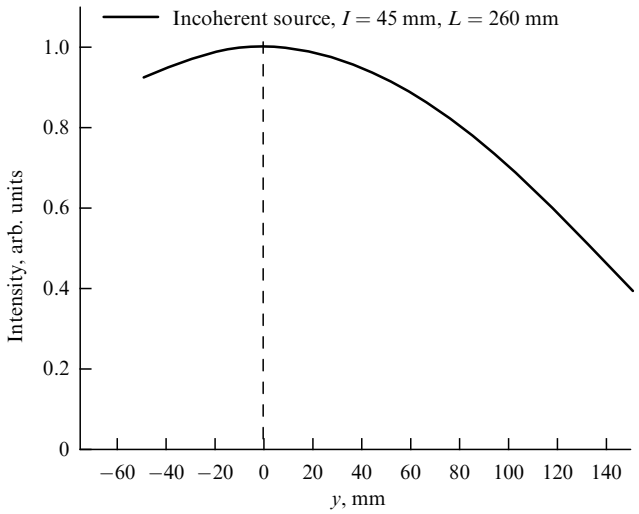

Figure 17. Intensity distribution on a screen when radiation from ferrite surface is incoherent (2.9).

magnetization of the ferrite: each small area of the ferrite surface becomes a source of coherent elementary electromagnetic waves. The radiating magnetic dipoles are oriented in the same way as the magnetic field that forms them, i.e., perpendicular to $\mathbf{J}_{\text{off}}$ and the normal to the ferrite surface **n**. Taking into account the geometry of the experiment, cylindrical elementary waves are emitted, which interfere with each other to produce the resultant radiation. If the magnetization of the surface layer of ferrite and the fronts of elementary waves propagate at the same speed, a common envelope of the wave fronts of elementary waves exists in a small neighborhood near the working surface of the ferrite prism, where the phases of elementary waves emitted by different parts of the ferrite surface coincide. In accordance with Huygens' principle, as a result of interference, elementary waves cancel each other everywhere, with the exception of their common envelope, where their intensities add up. Accordingly, the resulting radiation propagates with a small angular divergence parallel to the ferrite surface in the direction of the anode. The coherence of radiation, as in the case of the classical Vavilov–Cherenkov effect [25–27], is a consequence of the same excitation conditions for all emitters. This assumption can become a rigorous model of the process of generating electromagnetic radiation in the pre-breakdown stage of a discharge on the surface of the ferrite, provided that the magnetization wave propagates in the surface layer of the ferrite (a dielectric with a high value of magnetic permeability μ) at the same speed as the electromagnetic pulse above the surface of the dielectric. Otherwise, a common envelope for elementary waves will not be formed. We are reminded that, in the absence of surface conduction currents, the tangential components of the electromagnetic field (i.e., components parallel to the dielectric plane) near the discontinuity surface satisfy the conditions [28]

$$E_{2t} = E_{1t} , \qquad (2.10)$$

$$H_{2t} = H_{1t} , \qquad (2.11)$$

where E_{1t}, H_{1t}, are the components of the electric and magnetic fields in the surface layer of the dielectric, and

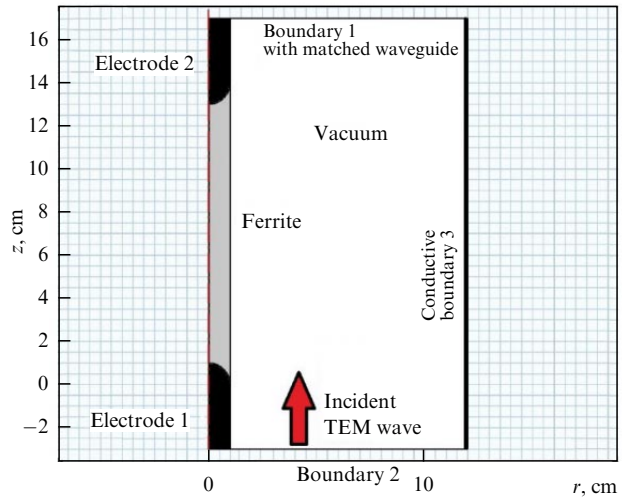

Figure 18. Section of a coaxial waveguide with a ferrite rod 2 cm in diameter with a half-plane passing through axis of waveguide. Diameter of central core of waveguide is 2 cm, internal diameter of braid is 24 cm.

E_{2t}, H_{2t}, are the components of the fields in the surface layer above the dielectric.

From relations (2.10), (2.11), it follows that electromagnetic pulses in the surface layer of the dielectric and above its surface move at the same speed. Note that the formation of magnetization is a material process associated with the ordering of the orientation of the magnetic moments of the atoms of a ferromagnet caused by the spin of the electrons. This process may take some time τ, which will ultimately lead to a time shift τ between the passage of the electromagnetic excitation pulse and the magnetization wave. Nevertheless, the speed of the magnetization wave must be the same as that of the exciting electromagnetic pulse; accordingly, the phases of the elementary waves emitted by different parts of the ferrite surface must coincide.

Using a special computer program (Comsol Multiphysics 6.1.), we analyzed the electrophysical processes that arise when pulsed electric fields pass through dielectrics with high values of magnetic permeability μ and permittivity ε [29]. A nonstationary electrodynamic problem was solved for the vector potential **A** of the magnetic field (notation in the SI system):

$$\nabla \times \mu_{\mathrm{r}}^{-1}(\nabla \times \mathbf{A}) + \mu_0 \sigma \frac{\partial \mathbf{A}}{\partial t} + \mu_0 \frac{\partial}{\partial t}\left(\varepsilon_0 \varepsilon_{\mathrm{r}} \frac{\partial \mathbf{A}}{\partial t}\right) = 0\,, \qquad (2.12)$$

where ε_0 and μ_0 are the dielectric and magnetic constants of vacuum, ε_{r} and μ_{r} are the relative permittivity and magnetic permeability of the sample. The computational domain is shown in Fig. 18. A solid ferrite rod 10 cm long and 2 cm in diameter was located between two hemispherical electrodes in the gap of the central core of a coaxial waveguide with an impedance of 149 Ω. The diameter of the central core was 2 cm, the internal diameter of the braid was 24 cm. A TEM wave passed through boundary 2 from the side of the first electrode (indicated in the figure). The boundary condition for boundaries 1 and 2 in the figure is a waveguide with an impedance of 149 Ω and along boundary 3 a superconducting surface.

We considered the passage of the following electrical pulses with a voltage amplitude $U_0 = 100$ kV.

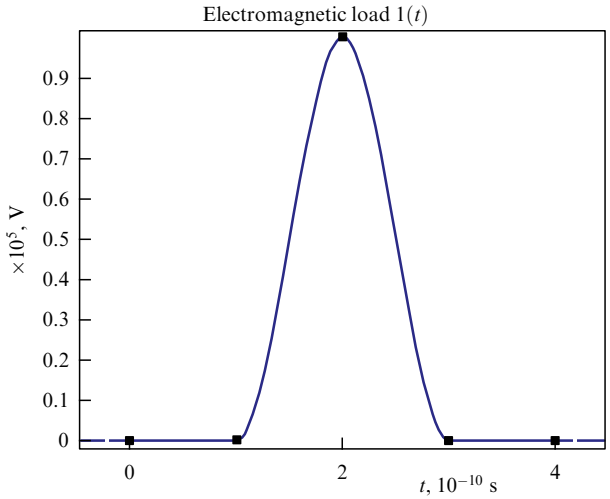

Figure 19. Voltage rise time: 0.1 ns. Voltage decay time: 0.1 ns. Total pulse duration: 0.2 ns.

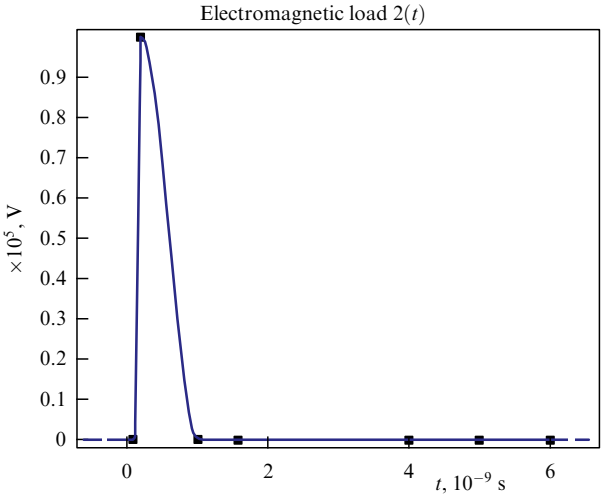

Figure 20. Voltage rise time: 0.1 ns. Voltage decay time: 0.1 ns. Total pulse duration: 1 ns.

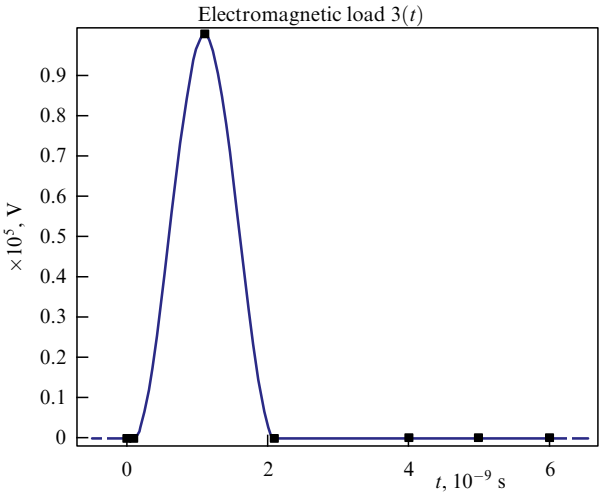

Figure 21. Voltage rise time: 1 ns. Voltage decay time: 1 ns. Total pulse duration: 2 ns.

The spatiotemporal dependence of the φ-component of magnetization I_φ (magnetic moment per unit volume of the dielectric) was analyzed. The calculations were carried out in

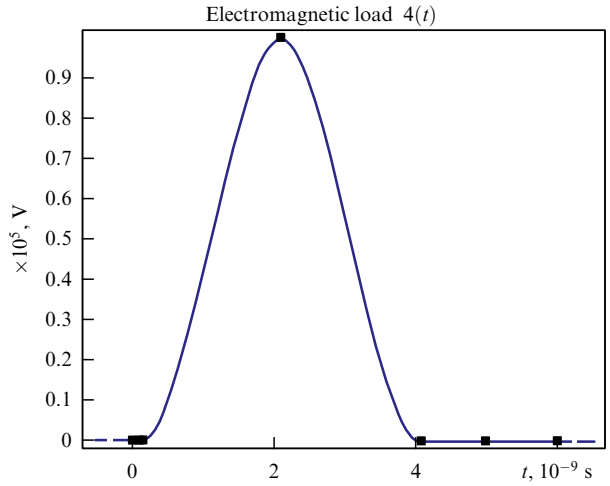

Figure 22. Voltage rise time: 2 ns. Voltage decay time: 4 ns. Total pulse duration: 4 ns.

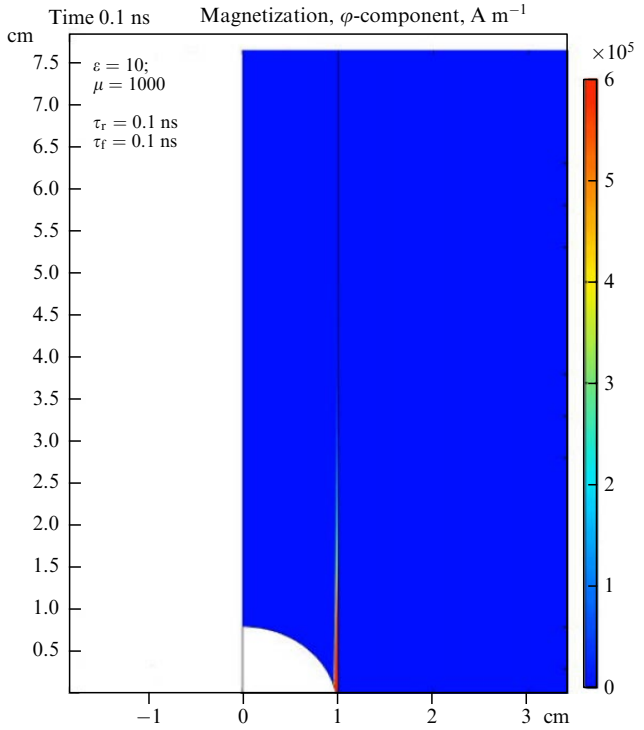

Figure 23. Picture of magnetization formation at point in time $t_1 = 0.1$ ns.

a cylindrical coordinate system (variables ρ, φ, z); the z-axis coincides with the axis of the cylinder and the waveguide.

As an example, Figs 23–25 serve to illustrate the magnetization formation pattern when a ferrite rod with $L = 10$, $\mu = 1000$, length $\varepsilon = 10$ cm, and a diameter of 2 cm was exposed to a voltage pulse (voltage rise and fall times $\tau_r = \tau_f = 0.1$ ns; pulse duration $\tau_r + \tau_f = 0.2$ ns; voltage amplitude $U_0 = 100$ kV; preliminary pulse parameters can be found in Figs 19–22). Figures 23–25 show the distribution of the φ-component of magnetization I_φ at a certain point in time along the cross section of a ferrite rod with a half-plane passing through the cylinder axis. Figure 23 corresponds to the point in time $t_1 = 0.1$ ns after the onset of the pulse. It can be seen from the figure that during this time a thin sub-millimeter near-surface magnetization layer of length $l\,(0.1\text{ ns}) = 3$ cm was formed; accordingly, the speed of propagation of the magnetization wave $v_m = c$. Figure 24 corresponds to the point in time $t_2 = 0.25$ ns. During this time, a near-surface thin layer of magnetization of length $l\,(0.25\text{ ns}) = 7.5$ cm was formed, in line with the speed of propagation of the magnetization wave $v_m = c$. Finally, Fig. 25 corresponds to the point in time $t_3 = 0.61$ ns. During this time, light travels a distance $l\,(0.61\text{ ns}) = 18.3$ cm, i.e., in the case of a rod of length $L = 10$ cm, the magnetization wave obviously reached the

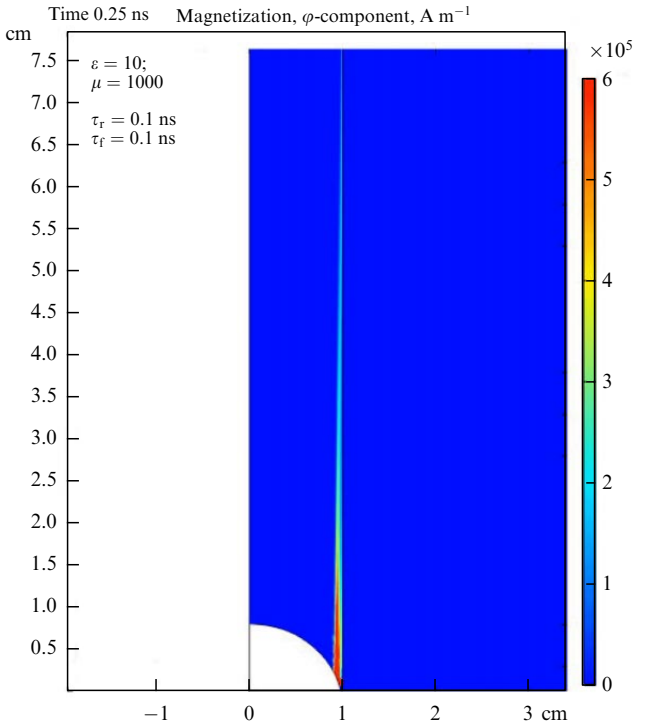

Figure 24. Picture of magnetization formation at point in time $t_2 = 0.25$ ns.

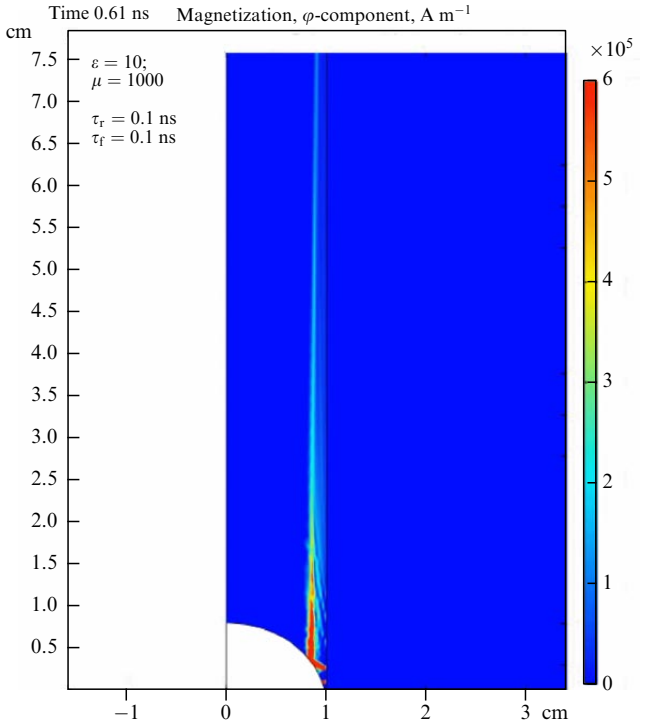

Figure 25. Picture of magnetization formation at point in time $t_3 = 0.6$ ns.

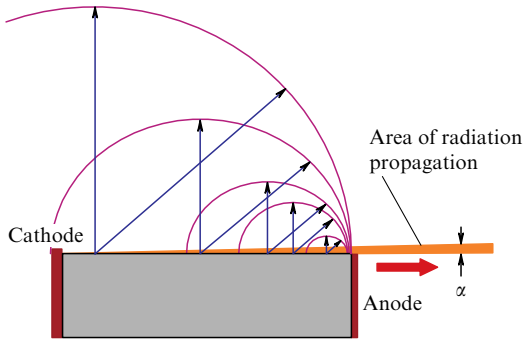

Figure 26. Diagram explaining formation of region of coherent radiation propagation.

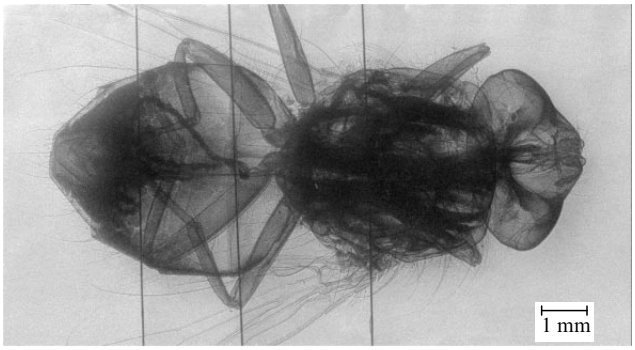

Figure 27. X-ray image of a house fly recorded using emission of X-pinch of four Nb wires with a diameter of 25 μm in radiation with an energy of $2.5 < E < 5$ keV.

opposite electrode. One can see that the layer with nonzero magnetization as a whole is contracted towards the axis of the ferrite cylinder; accordingly, the radiation that can be formed in it will be absorbed by the outer layer of the ferrite.

As a result, it was found that, during the passage of all the considered voltage pulses, the magnetization of the ferrite cylinder is formed in a narrow cylindrical submillimeter layer, first on the surface of the cylinder, and, upon reaching the magnetization wave of the opposite electrode, the layer as a whole contracts towards the axis of the cylinder. It is significant that the front of the magnetization wave in the surface layer moves at a speed c. For the ferrite sample under consideration, the values of the permittivity and magnetic permeability are $\varepsilon \sim 10$ and $\mu \sim 1000$. And if the speed of movement of the magnetization wave front is $v_m = c/\sqrt{\varepsilon\mu} = 0.01c$, then coherent addition of elementary electromagnetic waves emitted by different sections of the ferrite surface is out of the question.

Since, as shown above, the magnetization wave front and the elementary wave fronts propagate at the same speed, the common envelope of the wave fronts of the elementary waves exists in a small neighborhood near the working surface of the ferrite prism, where the phases of the elementary waves emitted by different parts of the ferrite surface coincide. Figure 26 shows a diagram explaining the formation of the radiation propagation region due to the coherent addition of elementary electromagnetic waves. In accordance with Huygens's principle, as a result of interference, elementary waves cancel each other everywhere, with the exception of their common envelope, where their intensities add up. Accordingly, the resulting radiation propagates with a small angular divergence parallel to the ferrite surface in the direction of the anode. Coherence of radiation, as in the case of the classical Vavilov–Cherenkov effect, is a consequence of identical excitation conditions for all emitters.

To a first approximation, we can assume that the longitudinal electric field strength E is proportional to the applied voltage U; accordingly, a narrowly directed pulse of electromagnetic radiation is formed when the displacement current $\mathbf{J}_{\text{off}} = (1/4\pi)(\partial\mathbf{E}/\partial t)$ reaches its maximum (see Fig. 11, curve *3*). It is easily shown that, for cylindrical waves in the case of coherent addition, the energy flux density P transferred by the pulse of the radiation under study

$$P(y, l, L) \sim \frac{l^2}{L}\left(\operatorname{sinc}\left[\frac{\pi y^2 l}{2\lambda L^2}\right]\right)^2, \qquad (2.13)$$

where y is the coordinate of a point in the observation plane, l is the length of the working part of the ferrite prism, and L is the distance from the end of the prism to the observation plane. (Relation (2.13) was obtained under the condition $L \gg l, y$.) In other words, the dependence of the energy flux density P on the length of the working part of the ferrite prism should be quadratic, which we observed experimentally with a fairly high accuracy.

3. Conclusion

In conclusion, we note that this study analyzed the properties of radiation generated by high-current nanosecond discharges. The first part of the paper is concerned with the feasibility of using a plasma source of soft X-ray radiation — the X-pinch. It turns out that the so-called hot spot (HS) of the X-pinch can have micron dimensions, and the radiation energy output is at the level of fractions or even units of joules with a pulse duration not exceeding a nanosecond. Such dimensions of the HS in a large number of cases make it possible to consider it a spatially coherent (i.e., point-like), high-brightness (with a brightness temperature $T_{\text{br}} \sim 10^7$ K) source of soft X-ray radiation. Spatial coherence plays an important role in the formation of images of non-self-luminous objects. When the high brightness temperature of the HS is taken into account, then, notably, any plasma object with a temperature up to $T_{\text{br}} \sim 10^6$ K can be considered a non-self-luminous object. Non-self-luminous objects are observed as a result of the scattering of waves incident on the object from extraneous light sources. If the source is point-like, then electromagnetic oscillations at all points of the illuminated object are in strictly defined phase relationships, i.e., coherent. Accordingly, in the image, too, it is necessary to add up not the intensities but the amplitudes of electromagnetic oscillations coming from various points of the object to a given image plane [9].

By way of example, Fig. 27 shows an image of a house fly recorded in the X-pinch radiation of four Nb wires with a diameter of 25 μm in radiation with an energy of $2.5 < E < 5$ keV. Source-to-film distance: 30 cm; source-to-subject distance: 7.5 cm; magnification: ×4. Use was made of the setup shown in Fig. 4 [8].

The X-ray image clearly shows micron-sized details of the internal structure of the fly, which should be practically transparent in the radiation of 2.5 to 5 keV used in these experiments. Therefore, the use of a spatially coherent soft X-ray source made it possible to obtain a high-quality image of the internal structure of a weakly absorbing biological object with submicron resolution without the use of focusing or limiting optical elements.

The second part of the paper describes an investigation of a new physical phenomenon involving the production of a short (< 2 ns), narrowly directed pulse of electromagnetic radiation in the pre-breakdown stage of a high-current discharge on the surface of ferrite, the X-ray region ($h\nu > 1$ keV) accounting for 50% of the energy spectrum. We emphasize the important feature and novelty of the phenomenon we are observing: there is no optically transparent medium with a refractive index n and there is no charge moving at a speed $v > c/n$. The radiation under study results from the passage of an exciting electromagnetic pulse over the surface of a ferrite prism during the formation of a longitudinal electric field in the interelectrode gap. This process leads to the appearance of a magnetization wave propagating in the submillimeter surface layer of the dielectric. Each small area of the ferrite surface becomes a source of elementary electromagnetic waves. The front of the magnetization wave and the resulting radiation move in the same direction at the same speed, and the propagation region is formed as a result of the coherent addition of elementary electromagnetic waves. As a result, due to interference, the total radiation from the entire surface is concentrated in a small spatial region, which explains the high intensity and directionality of the radiation without any focusing or limiting devices. As in the case of Cherenkov radiation, it is coherent, but not monochromatic. Each small area of the ferrite surface emits radiation with the same energy distribution (see Fig. 12) and a strictly fixed phase shift for each wavelength. In this case, no restrictions are imposed on the size of the source, unlike the case discussed in the first part of the study.

This study was supported by the Russian Science Foundation under grant no. 19-79-30086.

References

1. Zakharov S M, Ivanenkov G V, Kolomenskii A A, Pikuz S A, Samokhin A I, Ulshmid J "Wire X-pinch in a high current diode" *Sov. Tech. Phys. Lett.* **8** 456 (1982); "Provolochnyi X-pinch v sil'notochnom diode" *Pis'ma Zh. Tekh. Fiz.* **8** 1060 (1982)
2. Pikuz S A, Shelkovenko T A, Hammer D A "X-pinch. Part I" *Plasma Phys. Rep.* **41** 291 (2015); "X-pinch. Chast' I" *Fiz. Plazmy* **41** 319 (2015)
3. Pikuz S A, Shelkovenko T A, Hammer D A "X-pinch. Part II" *Plasma Phys. Rep.* **41** 445 (2015); "X-pinch. Chast' II" *Fiz. Plazmy* **41** 483 (2015)
4. Shelkovenko T A, Sinars D B, Pikuz S A, Hammer D A "Radiographic and spectroscopic studies of X-pinch plasma implosion dynamics and X-ray burst emission characteristics" *Phys. Plasmas* **6** 1305 (2001)
5. Song B M, Pikuz S A, Shelkovenko T A, Hammer D A "Determination of the size and structure of an X-pinch X-ray source from the diffraction pattern produced by microfabricated slits" *Appl. Opt.* **44** 2349 (2005)
6. Sinars D B, Pikuz S A, Shelkovenko T A, Chandler K M, Hammer D A "Temporal parameters of the X-pinch X-ray source" *Rev. Sci. Instrum.* **72** 2948 (2001)
7. Pikuz S A, Shelkovenko T A, Sinars D B, Hammer D A "Temporal characteristics of X-ray emission from X-pinches" *Plasma Phys. Rep.* **32** 1020 (2006); "Vremennye kharakteristiki rentgenovskogo izlucheniya X-pincha" *Fiz. Plazmy* **32** 1106 (2006)
8. Shelkovenko T A, Pikuz S A, Hammer D A "A review of projection radiography of plasma and biological objects in X-pinch radiation" *Plasma Phys. Rep.* **42** 226 (2016); "Proektsionnaya rentgenografiya plazmennykh i biologicheskikh ob'ektov v izluchenii X-pincha (Obzor)" *Fiz. Plazmy* **42** 234 (2006)
9. Landsberg G S *Optika* (Optics) (Moscow: Fizmatlit, 2010) p. 848
10. Tilikin I N, Tskhai S N, Shelkovenko T A, Savinov S Yu, Pikuz S A "Generation of intense UV radiation during high-current breakdown over a ferrite surface" *Plasma Phys. Rep.* **44** 600 (2018)
11. Tilikin I N, Tzhai S N, Shelkovenko T A, Savinov S Yu, Pikuz S A, Mingaleev A R "A pulsed, high-intensity source of XUV radiation based on ferrite surface breakdown at high current" *IEEE Trans. Plasma Sci.* **46** 3982 (2018)
12. Tilikin I N, Savinov S Yu, Pestovskii N V, Pikuz S A, Tskhai S N, Shelkovenko T A, Dushkin G A "Coherent x-ray radiation induced by high-current breakdown on a ferrite surface" *J. Phys. D* **55** 405006 (2022)
13. Watanabe K, Furusho K, Kashiwabara S, Fujimoto F "Characteristics of x-ray radiation by a nonequilibrium electron flow emerged from a formed ferrite filament" *J. Appl. Phys.* **68** 5059 (1990)
14. Kozyrev A V et al. "Soft X-ray generation and its role in breakdown of air gap at elevated pressures" *Tech. Phys. Lett.* **37** 1054 (2011); "Generatsiya myagkogo rentgenovskogo izlucheniya i ego rol' v razvitii proboya vozdushnogo promezhutka pri povyshennykh davleniyakh" *Pis'ma Zh. Tekh. Fiz.* **37** (22) 26 (2011)
15. Sorokin D A et al. "X-ray radiation and runaway electron beams generated during discharges in atmospheric-pressure air at rise times of voltage pulse of 500 and 50 ns" *Laser Part. Beams* **36** (2) 186 (2018)
16. Kochkin P et al. "Analyzing x-ray emissions from meter-scale negative discharges in ambient air" *Plasma Sources Sci. Technol.* **25** 044002 (2016)
17. Agafonov A V et al. "Anisotropy in hard bremsstrahlung from a high-voltage laboratory simulation of an atmospheric discharge" *Plasma Sources Sci. Technol.* **28** 095014 (2019)
18. Spielman R B, Ruggles L E, Pepping R E, Breeze S P, McGurn J S, Struve K W "Fielding and calibration issues for diamond photoconducting detectors" *Rev. Sci. Instrum.* **68** 762 (1997)
19. Mesyats G A, Korovin S D, Sharypov K A, Shpak V G, Shunailov S A, Yalandin M I "Dynamics of subnanosecond electron beam formation in gas-filled and vacuum diodes" *Tech. Phys. Lett.* **32** 18 (2006); "O dinamike formirovaniya subnanosekundnogo elektronnogo puchka v gazovom i vakuumnom diode" *Pis'ma Zh. Tekh. Fiz.* **32** (1) 35 (2006)
20. Mesyats G A, Yalandin M I "High-power picosecond electronics" *Phys. Usp.* **48** 211 (2005); "Pikosekundnaya elektronika bol'shikh moshchnostei" *Usp. Fiz. Nauk* **175** (3) 225 (2005)
21. Katz L, Penfold A S "Range-energy relations for electrons and the determination of Beta-ray end-point energies by absorption" *Rev. Mod. Phys.* **24** 28 (1952)
22. Andreev S N, Bernatskiy A V, Dushkin G A, Tskhai S N, Pikuz S A, Tilikin I N, Shelkovenko T A, Savinov S Yu "Spatial characteristics of radiation initiated by a discharge over the ferrite surface" *Bull. Lebedev Phys. Inst.* **48** 321 (2021); "Prostranstvennye kharakteristiki izlucheniya, initsiiruemogo razryadom po poverkhnosti ferrita" *Kratk. Soobshch. Fiz.* **48** (10) 43 (2021)
23. "Filter Transmission," The Center for X-Ray Optics at Lawrence Berkeley National Laboratory, https://henke.lbl.gov/optical_constants/filter2.html
24. Born M, Wolf E *Principles of Optics*: *Electromagnetic Theory of Propagation, Interference, and Diffraction of Light* 2nd rev. ed. (London: Pergamon Press, 1964); Translated into Russian: *Osnovy Optiki* (Moscow: Nauka, 1970)
25. Cerenkov P A *C.R. Acad. Sci. USSR* **2** 451 (1934); *Dokl. Akad. Nauk SSSR* **2** 451 (1934); *Usp. Fiz. Nauk* **93** 385 (1967)
26. Čerenkov P A "Visible radiation produced by electrons moving in a medium with velocities exceeding that of light" *Phys. Rev.* **52** 378 (1937)
27. Tamm I E, Frank I M *C.R. Acad. Sci. USSR* **14** 109 (1937); *Dokl. Akad. Nauk SSSR* **14** 107 (1937); *Usp. Fiz. Nauk* **93** 388 (1967)
28. Tamm I E *Fundamentals of the Theory of Electricity* (Moscow: Mir Publ., 1979) Translation into English from Russian 9th ed.; *Osnovy Teorii Elektrichestva* 11th Russian ed., rev. and enlarg. (Moscow: Fizmatlit, 2003) p. 425–426
29. Petrov A A, Klimovich S M, Pestovskii N V, Tilikin I N, Savinov S Yu "Formation of the magnetization wave in the prebreakdown discharge stage over the ferrite surface" *Bull. Lebedev Phys. Inst.* **50** (11) 503 (2023); "Formirovanie volny namagnichennosti v predproboinoi stadii razryada po poverkhnosti ferrita" *Kratk. Soobshch. Fiz.* **50** (11) 73 (2023)